



Effect of Pulse Current Frequency on Microstructure and Hot Corrosion Behavior of Tungsten Inert Gas-Welded Joints of N155 Superalloy

Amirkeyvan Rahimi, Morteza Shamanian, and Masoud Atapour

Submitted: 15 December 2020 / Revised: 28 April 2021 / Accepted: 3 May 2021 / Published online: 17 May 2021

Thin sheets of N155 superalloy with Inconel 718 filler metal were welded using tungsten inert gas (TIG) process with different frequencies of the pulse current system. The present study aims to compare the hot corrosion resistance of the weld metal of samples with different frequencies in 90% Na₂SO₄-10% NaCl molten salt environment at 950±5 °C. The results of the hot corrosion test indicated that the sample with optimal frequency (240 Hz) could form the alternate protective layers (Cr₂O₃ and NiO) that prevented the interference of the iron element during the hot corrosion; therefore, the amount of damage to the substrate was reduced, and it made the parabolic rate constant (Kp) lower (up to 6h: 1.87 and after 6h: 0.186 (×10^{−10}) g².cm^{−4}.s^{−1}) than other welded specimens. In other welded specimens, due to the formation of poor and rich areas of chromium and nickel key elements, resulting from elements segregation of welding solidification, the weld metal surface was not uniformly corroded and the iron element created porous and brittle Fe₃O₄ oxide layers.

Keywords hot corrosion, inconel 718 filler, N155 superalloy, optimum frequency, parabolic rate constant (Kp), tungsten inert gas (TIG)

1. Introduction

N155 base-iron superalloy is used for many industrial applications; for instance, air- and land-based turbine engines and afterburner components, and some of them include aircraft tail cones, tail pipes and nozzles (Refs 1, 2). High temperatures with the environment that include pollutants such as sulfur, sodium, vanadium and different halides need special attention with regard to hot corrosion (Refs 3), which is one of the most important phenomena that can cause significant damages to N155 base-iron superalloys in combustion chambers and transfer chimneys. Thus, hot corrosion investigation of this superalloy is important in corrosive environments, especially in sulfide environments. Superalloys have been utilized in high-temperature applications, but they cannot provide the requirements of both the high-temperature erosion–corrosion resistance and the high-temperature strength at the same time (Refs 4-6). Hence, metals such as refractory stainless steels and nickel-based superalloys were developed, in which hot corrosion resistance is increased by adding chromium and other elements such as molybdenum, silicon and aluminum, which are combined with oxygen to create layers of Cr₂O₃, Al₂O₃ and SiO₂, which can protect the alloys from factors such as oxidation, sulfidation, nitrification and even carburization at

high temperatures (Refs 7-9). Generally, hot corrosion occurs in the environment of molten salts such as NaCl, V₂O₅ and Na₂SO₄, which are melted at temperatures above 650 °C and form the deposits that destroy protective or passive layers (Ref 3). The severity of hot corrosion depends on factors including chemical composition of sediments formed on metals, atmosphere, temperature and its changes, erosion, chemical composition and microscopic structure of metals. Hot corrosion can occur when the surface of a metal is partially or completely wetted by molten salt (Refs 10, 11). Sequeira et al. (Ref 12) found out that adding NaCl (up to 15%) to Na₂SO₄ has little effect on hot corrosion, but around 15-35% NaCl is more effective. Gurrappa et al. (Ref 13) figured out that Mo is primarily added for high-temperature strength in superalloys and not for hot corrosion resistance. Smart coatings are essential in improving hot corrosion resistance (Ref 13). Hot corrosion studies were performed on IN718 and IN738LC superalloys with three different salt mixture depositions of Na₂SO₄, NaCl, and V₂O₅/NaVO₃ at different temperatures, revealing that three salt mixtures importantly accelerate the oxidation behavior (Refs 14-18).

Some researchers tried to refine the microstructure and enhance the properties of the fusion zone using the PC-GTAW process. They figured out that performing the pulsed current causes a dramatic rise in finer equiaxed dendrites instead of columnar dendrites or cellular structure (Refs 19-21). Rahimi et al. (Refs 22, 23) figured out that using pulse current system is the simplest technique among different molten pool vibration techniques that are flexible and economical in welding industry. A sudden decrease in electric arc energy during the background current alternation of PC-GTAW makes the weld pool temperature decrease and the molten metal undergo undercooling conditions. In this condition, surface nucleation rises and the nuclei can be permanent due to the lower temperature in the background current alternation (Ref 23). Kumar et al. (Ref 24) found out that a mixed cellular structure and the columnar dendritic structure could be seen near the fusion line, while the

Amirkeyvan Rahimi, Morteza Shamanian, and Masoud Atapour, Department of Materials Engineering, Isfahan University of Technology, 8415683111 Isfahan, Iran. Contact e-mail: amir.keyvan73@gmail.com.

Table 1 Compositions of the base metal and the filler metal (wt.%)

Wt. %	C	Si	Mn	Cr	Co	Ni	Mo	W	Nb	Al	Ti	Fe
N 155 (Base metal)	0.12	1	1.5	21.5	20	21	3	2.5	1	Bal.
Inconel 718 (filler metal)	0.08	0.35	0.35	19	1	52.5	3.1	...	5.1	0.5	0.9	Bal.

Table 2 TIG welding parameters in this work (Ref 26)

Parameter	Value
Shielding/purging gas	99.999% pure argon
Shielding gas flow rate	12 L.min ⁻¹
Purging gas flow rate	15 L.min ⁻¹
Filler rod diameter	1.6 mm
Welding electrode	AWS A5.12 EWTH-2 (98% W + 2% ThO ₂)
Electrode diameter	1.6 mm
Polarity	Direct current electrode negative (DCEN)
Voltage	7.8 V
Welding speed	4 cm.min ⁻¹

equiaxed dendritic structure was observed in the center of the fusion zone. Jula et al. (Refs 25) figured out that the pulsed current system caused finer and equiaxed dendrites in the fusion zone. Moreover, the chemical analysis of the dendritic and interdendritic zones indicated that the segregation of alloy elements happens in the entire weld metals and that it is more severe with the constant current.

There is a relevant research in which thin sheets of N155 alloy with austenitic nickel-base filler metal (IN 718) were welded by different frequencies of the pulse current technique (Refs 26, 27). Rahimi et al. (Ref 26) found out that increasing the frequency up to the optimal level (240 Hz) expands the region of fine equiaxed grains that include equiaxed dendrites. Moreover, it limits the growth of epitaxial grains that consist of columnar dendrites. Only limited published literature has been reported on N155 superalloy (Refs 26, 27). The importance of this study is that using parabolic graph of corrosion kinetics and the EDS technique makes it possible to see the effect of pulse current frequency on hot corrosion resistance of the joint as well as that of chemical composition of N155 base-iron superalloy as base metal and IN718 filler metal.

2. Experimental

2.1 Welding Process

In this study, thin sheets of N155 superalloy were welded using IN718 filler metal (Table 1). The purpose of the study is to examine the effect of frequency on the microstructure and hot corrosion of tungsten inert gas (TIG)-welded joints. A PSQ-400A Model was used to perform the TIG welding process. The temperature of the samples was considered to be about 25 °C before welding. The argon gas was used for 5 and 25 seconds before starting the arc (pre-gas) and after applying the arc (post-gas), respectively, to clean and protect the molten pool. Parameters of the welding process are presented in Table 2.

In addition, four specimens with different frequencies and one sample with a constant current (18 A) without a frequency were joined (Fig. 1 and Table 3) (Ref 26).

2.2 Hot Corrosion Test

For the hot corrosion test, samples of the weld metal, the filler and the base metal were cut separately, and their surfaces were prepared to the polishing stage. The dimensions of the specimens for the hot corrosion test were 2 × 0.7 × 0.06 cm. The samples were cleaned in acetone, ethanol and distilled water in sequence in an ultrasonic bath before the test. Surfaces of the samples were smeared with 3 mg/cm² of the supersaturated salt solution (90% Na₂SO₄-10% NaCl), which could indicate a corrosive sulfide environment. Then, the samples were placed into alumina boats. After that, the alumina boats were placed in an oven at 110 °C for one hour to remove the moisture. Both the specimens and alumina boats were weighed by digital weighing balance Mettler Toledo-AG245 of 0.01 mg accuracy. Next, they were placed in the furnace at 950 °C (operating temperature range of this alloy in industry). All samples were weighed for each time of exposure. Times of exposure were 1, 2, 4, 6, 10, 15, 20, 24, 28, 32, 36, 40, 44 and 48 h. The kinetics of corrosion was analyzed from data of weight change measurements. The data were divided by the dimensions of initial surface (2 × 0.7 cm²) to form weight gain per unit area (mg/cm²) versus time (*t*) plot (Fig. 4a) for each sample. Then, the achieved data were squared to form the weight gain square (mg²/cm⁴) versus time (*t*) plot (Fig. 4b). Finally, surfaces of the corroded specimens were examined by Hitachi SU6600 scanning electron microscopy (SEM) equipped with energy-dispersive X-ray spectroscopy (EDS). In addition, corrosion products of the specimens were collected to characterize phase using X-ray diffraction (XRD) test. The results of hot corrosion test can indicate the effect of pulse current frequency on hot corrosion resistance of the joint as well as that of chemical composition of the base metal and the filler metal. Image J software was used in order to calculate the average sizes of dimples.

3. Results

3.1 Visual Observations

According to Fig. 2, the cross sections of all the welded samples can be seen that demonstrate full penetration for each sample. It should be noted that the welded sheet was very thin (0.6 mm), and the aim of the study is to join the thin sheets that created low weld width.

Based on Fig. 3, the hot corrosion product of two samples with green color can be seen after 48 h at 950 °C of the furnace. It is the nickel oxide (NiO), which appears as grown green grass. Eliaz et al. (Ref 3) found out that the dominant salt in

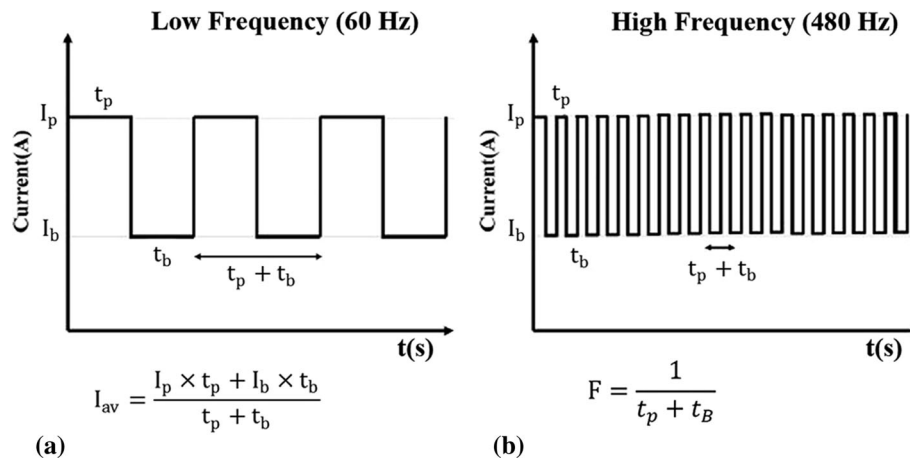


Fig. 1 Plots of typical pulse characteristics (Current versus. Time plot) at different frequencies; (a) low frequency (60 Hz), (b) high frequency (480 Hz)

Table 3 Values of the pulse frequency (F) of the welded samples (Ref 26)

Sample	I_p , (A)	I_b , (A)	t_p , (s)	t_b , (s)	F = Pulse frequency, (Hz)
T1	20	10	0.5	0.5	60
T2	20	10	0.5	0.5	120
T3	20	10	0.5	0.5	240
T4	20	10	0.5	0.5	480
T5	18	18

high temperature hot corrosion (HTHC) is Na_2SO_4 due to its high thermodynamic stability. The macroscopic appearance of HTHC is determined in many cases by severe peeling of the metal and by important color changes (greenish tone, resulting from the formation of NiO) in the region of the accelerated attack (Ref 3).

3.2 Corrosion Kinetics

Figure 4(a) shows weight gain per unit area for the salt-coated samples subjected to 950 ± 5 °C for 48 h. The salt-coated specimens show the parabolic behavior for all over the process of hot corrosion. The weight gain square (mg^2/cm^4) versus time (h) plot (Fig. 4b) was used to create rate law for the hot corrosion. According to Fig. 4b, the curves of weight gain square plot can be fitted by linear least-square procedure. Pilling and Bedworth (Ref 28) equation, $(\text{DW}/A)^2 = K_p \cdot t + C$, can be used to calculate the parabolic rate constant K_p in which DW/A is the weight gain per unit surface area (mg/mm^2), t stands for the time of exposure, and C shows a constant. Table 4 gives information about determined values of the parabolic rate constant (K_p) for the hot corroded samples.

Hot corrosion includes two stages: initiation and propagation. In the initial stage, chemical composition of the superalloy changes to pave the way for rapid corrosion. Changing the chemical composition includes the discharge of the chromium element from the base metal substrate, and the formation of sulfide layers on the alloy surface by passing sulfur through the shell, dissolving the oxides into the molten salt that expands the growth stresses, forms the channels and cracks in the oxide shell and creates porous oxide shells (Refs 29, 30). According

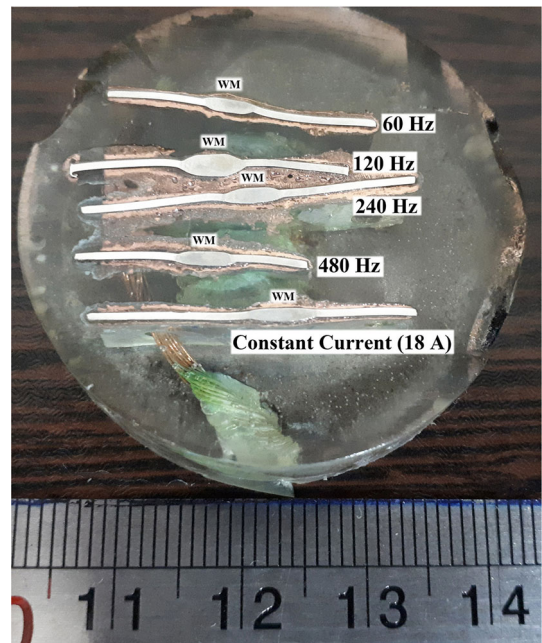


Fig. 2 Image of the cross sections of the welded specimens

to Table 4, both stages can be seen as changing in the parabolic rate constant (K_p) for the hot corroded samples, which vary after specific hours for each of them.

Based on Table 4 and Fig. 4, it can be seen that parabolic rate constants (K_p) of the hot corroded welding samples (T_1 to T_5) in both stages are almost close to each other; however, K_p of sample T_3 is lower (up to 6h: 1.87 and after 6h: 0.186 ($\times 10^{-10}$) $\text{g}^2 \cdot \text{cm}^{-4} \cdot \text{s}^{-1}$) than other welded specimens, and this sample went to the second stage earlier (after 6h). In addition, K_p of sample T_5 is higher (up to 10 h: 1.99 and after 10 h: 0.22 ($\times 10^{-10}$) $\text{g}^2 \cdot \text{cm}^{-4} \cdot \text{s}^{-1}$) than other welded samples. The least amount of K_p exists for the filler metal sample (up to 6h: 1.7 and after 6h: 0.175 ($\times 10^{-10}$) $\text{g}^2 \cdot \text{cm}^{-4} \cdot \text{s}^{-1}$), while the largest amount of K_p belongs to the base metal specimen (up to 15 h: 4.28 and after 15 h: 0.417 ($\times 10^{-10}$) $\text{g}^2 \cdot \text{cm}^{-4} \cdot \text{s}^{-1}$). For these issues, there are some metallographic reasons that will be mentioned in the details in the discussion part.

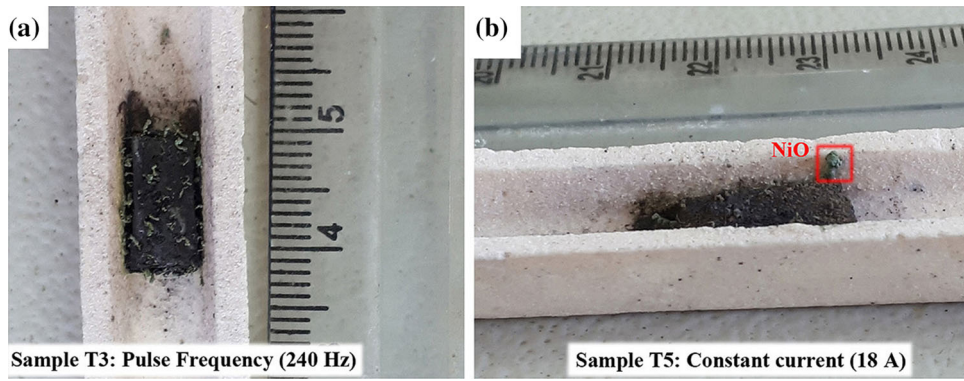


Fig. 3 Image of hot-corroded samples in alumina boats; (a) sample T_3 (240 Hz), (b) sample T_5 (constant current (18 A))

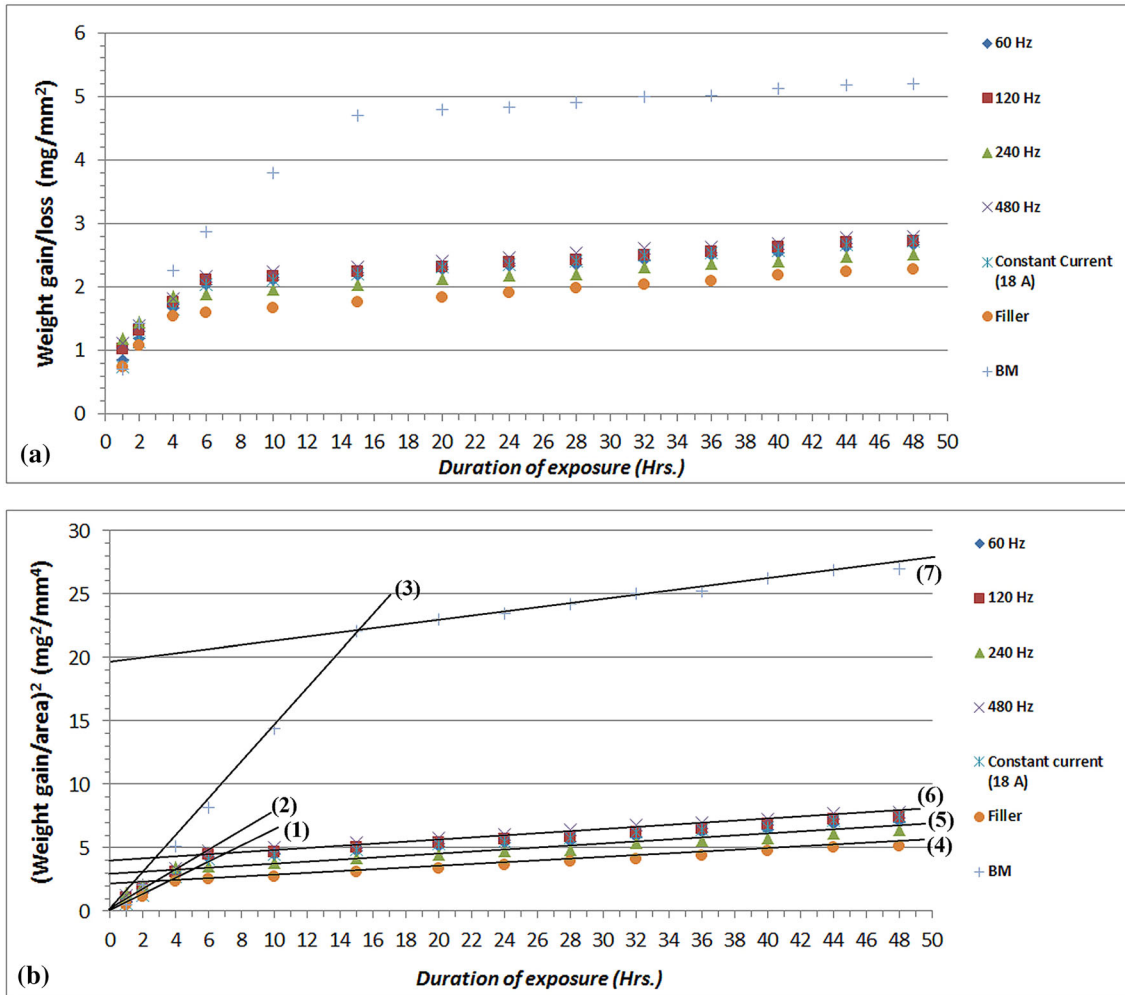


Fig. 4 Plots of hot corroded specimens exposed for 48 h at 950 ± 5 °C; (a) weight gain/area versus duration of exposure plot, (b) (weight gain/area)² versus duration of exposure plot

Table 4 Values of the parabolic rate constant (Kp)

Samples	T_1	T_2	T_3	T_4	T_5	FM	BM
$K_p (\times 10^{(-10)} \text{ g}^2 \cdot \text{cm}^{-4} \cdot \text{s}^{-1})$	1.91 (up to 10h)	1.9 (up to 10h)	1.87 (up to 6h)	1.93 (up to 10h)	1.99 (up to 10h)	1.7 (up to 6h)	4.28 (up to 15h)
	0.192 (after 10h)	0.2 (after 10h)	0.186 (after 6h)	0.21 (after 10h)	0.22 (after 10h)	0.175 (after 6h)	0.417 (after 15h)

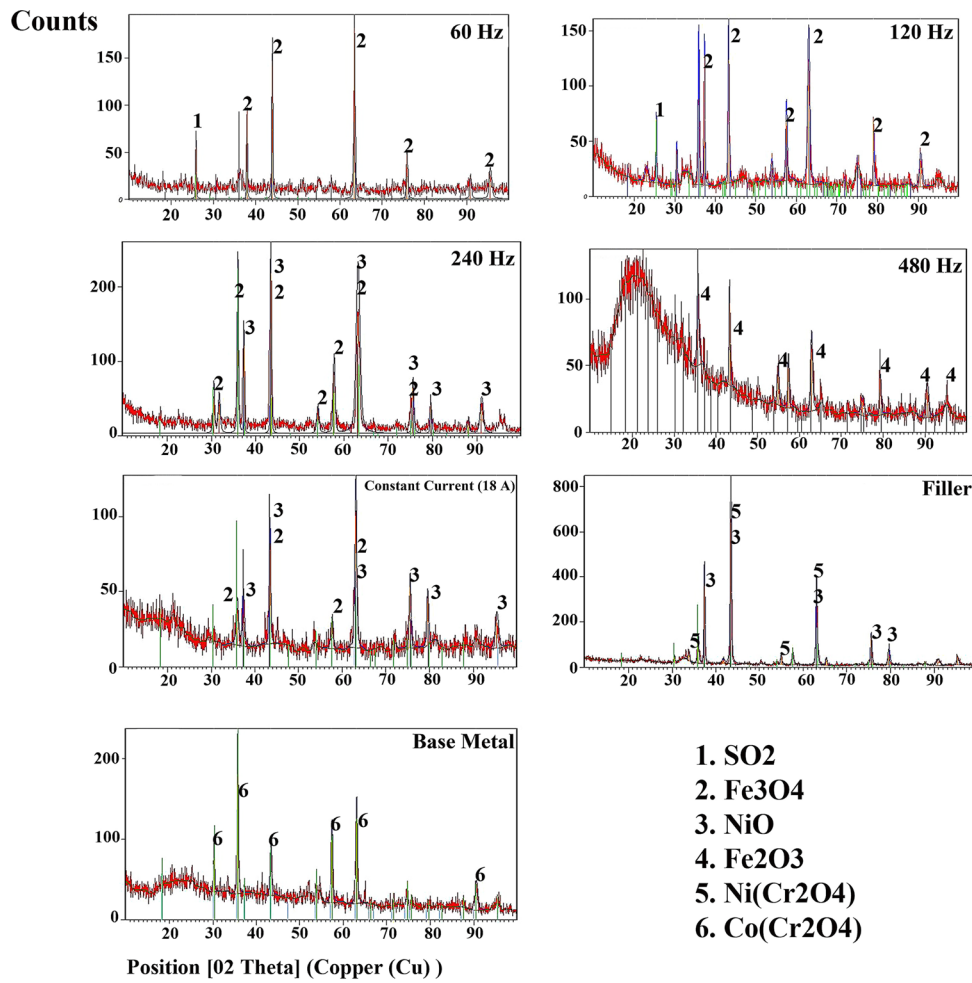


Fig. 5 X-ray diffraction (XRD) analysis of the hot corrosion products of the welded samples after 48 hours at 950 ± 5 °C

3.3 XRD Analyses

The peaks related to Fe₃O₄ can be seen in the XRD analysis of the corrosion products of *T*₁ and *T*₂ (Fig. 5). Sample *T*₃ shows peaks related to Fe₃O₄ phase with less intensity as well as NiO phase with high percentage that indicates the dominant phase of the corrosion product. Apart from that, most corrosion products of the two samples *T*₄ and *T*₅ contain iron oxide phase that indicates the involvement of the iron element in the hot corrosion due to the weak protection of chromium and nickel oxide layers (NiO and Cr₂O₃). A high amount of the brittle oxide layer of Co(Cr₂O₄) can be observed in the X-ray diffraction analysis of the corrosion products of the base metal sample.

4. Discussion

According to Fig. 6a and b, the large columnar dendrites can be seen at 60 and 120 Hz while increasing the frequency up to the optimal level (240 Hz) expands the region of fine equiaxed dendrites (Fig. 6c) (Ref 26). The presence of more equiaxed dendrites indicates a large dendritic fragmentation (Ref 25). Raising the frequency above the optimal level (480 Hz) leads to a lack of uniformity of microstructure in the weld metal (Fig. 6d). In fact, at high frequency, the thermal fluctuation and

the domains of the oscillations induced in the molten pool are extremely decreased (Ref 26). Using constant current (18 A) with higher heat input (136 J/mm) causes the expansion of the columnar dendrites (Fig. 6e) (Ref 26).

Filler metal and welded samples *T*₁ to *T*₅ have higher amounts of nickel element (about 50%) than the N155 base metal (about 20%) due to the use of Inconel 718 filler metal for welding. Instead of that, the base metal has a higher amount of cobalt element (about 20%), and the amount of chromium element as the main component of the Cr₂O₃ protective layer is approximately similar to that in the welded samples (see Table 1). Thus, the elements mentioned in the chemical composition of the samples play an important role in the formation of oxide layers, and differences in their amounts can also lead to differences in the hot corrosion resistance of the specimens in the same corrosive environment.

According to Table 1, since the base metal and filler metal have small amounts of refractory elements such as molybdenum and tungsten (about 2-3%), acidic fluxing of refractory oxides does not happen; since they also have negligible percentages of aluminum and niobium components, these elements do not affect hot corrosion in this study. Goebel et al. (Ref 31) reported that acidic fluxing is affected by alloy, and acidic conditions in the salt are characterized by the dissolution of alloying agents that have a great desire to be combined with (O²⁻) or Na₂O. This acidic fluxing is usually the result of the

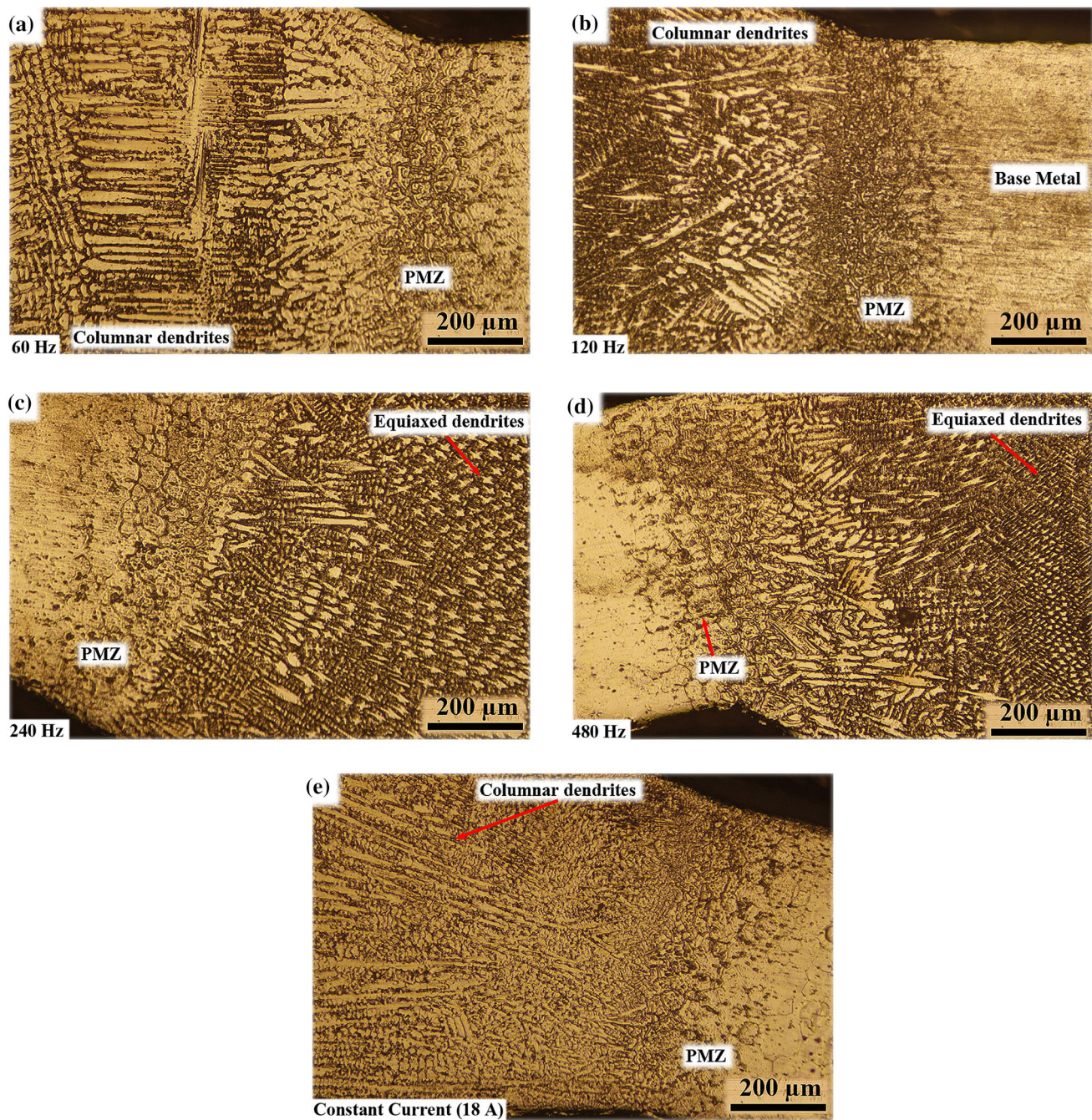


Fig. 6 Microstructure of the weld metal, HAZ and interface of: (a) T_1 (60 Hz), (b) T_2 (120 Hz), (c) T_3 (240 Hz), (d) T_4 (480 Hz), (e) T_5 (constant current (18 A))

dissolution of refractory metal oxides in sodium sulfate (such as molybdenum, tungsten and vanadium, which form molybdate, tungstate and vanadate, respectively), which reduces the concentration of oxygen ion (O^{2-}) in the molten salt (Ref 31).

According to SEM images of corroded cross sections and EDS linear analysis (Fig. 7a and b), it can be seen that in specimens T_1 and T_2 with pulse frequencies of 60 Hz and 120 Hz, the two key elements of chromium and nickel made the internal protective adhesive oxide layers (Cr_2O_3 and NiO) and the iron element created porous and brittle Fe_3O_4 oxide layers (Fig. 5). There is an important point that the amount of Cr in the superalloy was not enough to cover the whole surface with continuous Cr_2O_3 layer. Due to the external layer of other

oxides, like FeO, internal precipitates of Cr_2O_3 were created in other regions of the superalloy surface (Ref 32, 33).

Sample T_3 has a uniform metal–shell interface with smooth and dense oxide shells that are NiO and Cr_2O_3 , respectively, and there is no trace of porous and brittle outer shell of Fe_3O_4 (Fig. 5 and 7c). It should be noted that the existence of Cr_2O_3 sharply speeded up the dissolution of Fe_2O_3 . Therefore, the kinetics of dissolution of Cr_2O_3 in the presence of Fe_2O_3 was much quicker than that for Cr_2O_3 alone (Ref 33), which is consistent with the analysis of the kinetics of hot corrosion of the welded samples (Fig. 4). Thus, synergistic dissolution could be seen clearly for these oxides. An even more intensive result should be expected for co-presence of very acidic oxides in

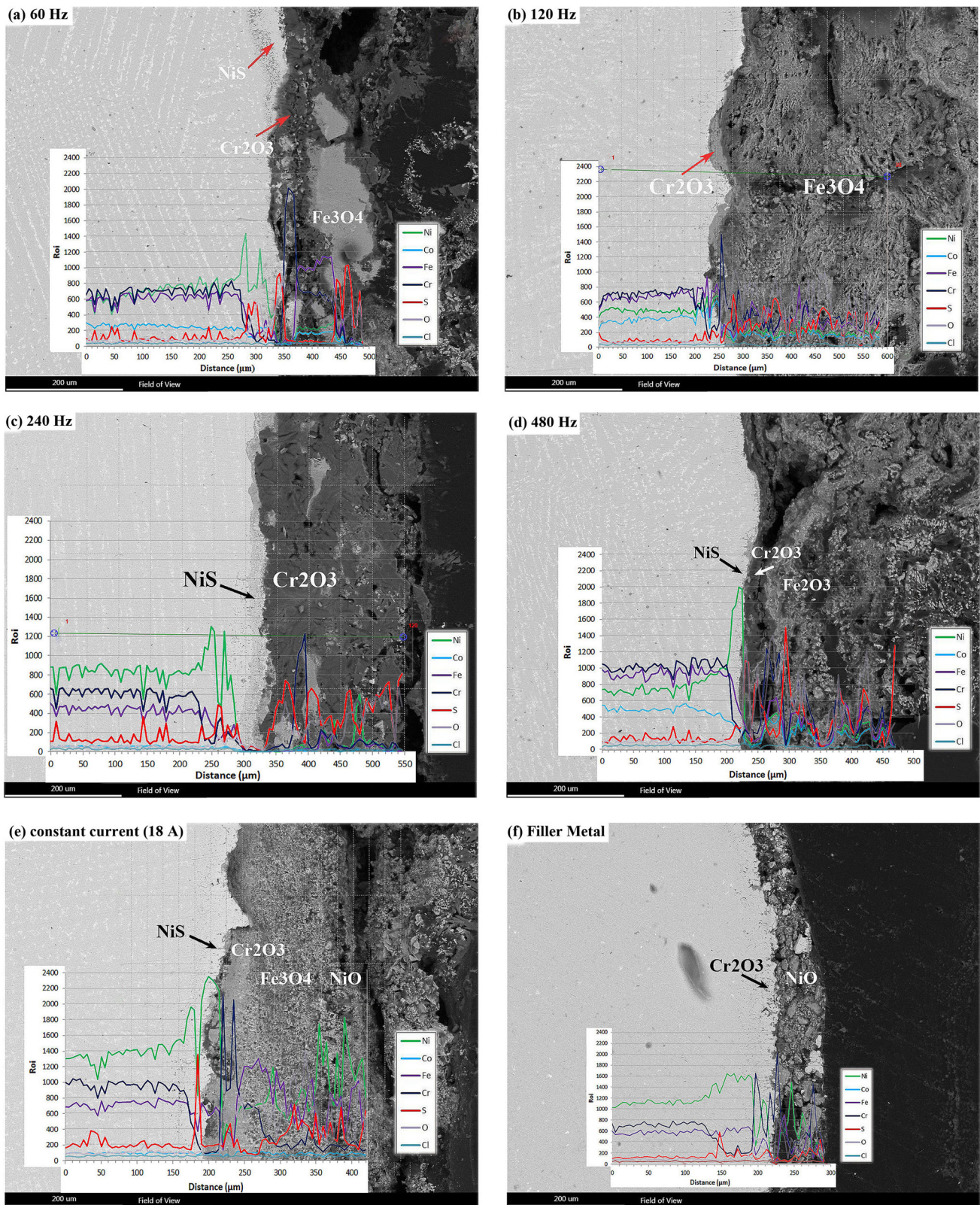


Fig.7 SEM image of the corroded cross section of welded specimens after 48 hours of the hot corrosion test at 950 ± 5 °C with the EDS linear analysis; (a) T_1 (60 Hz), (b) T_2 (120 Hz), (c) T_3 (240 Hz), (d) T_4 (480 Hz), (e) T_5 (constant current (18 A)), (f) filler metal

combination with very basic oxides (Ref 34). Moreover, it can be shown that the Cr-depletion area is characterized clearly near the inner corrosion layer. The variation between two layers can be described as the oxide dissolution/re-precipitation mecha-

nism [35]. The corroded cross section of sample T_4 (480 Hz), like those of samples T_1 and T_2 , has an outer porous shell of Fe_2O_3 with internal protective adhesive oxide layers of Cr_2O_3 and NiO (Fig. 7d). Welded specimen of T_5 with the constant

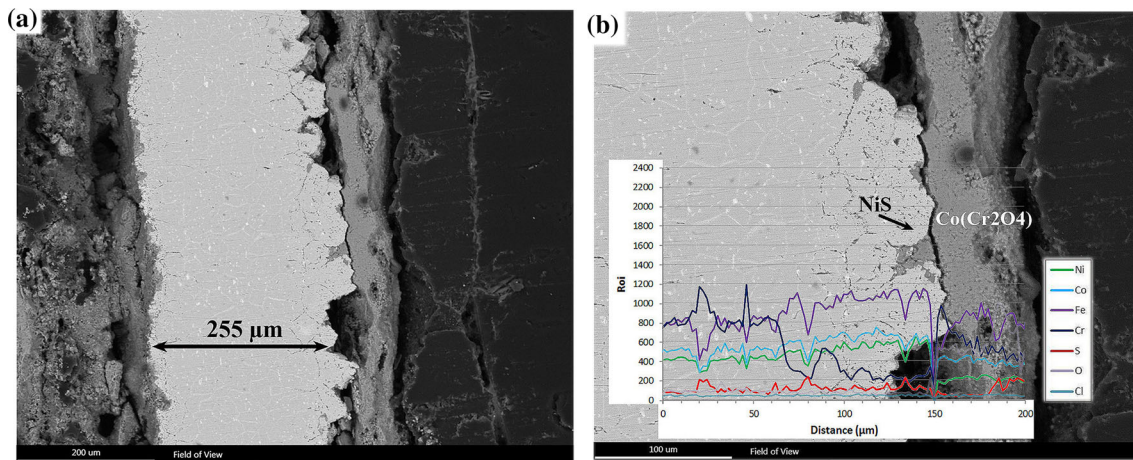


Fig. 8 SEM image of the corroded cross section of the base metal sample after 48 hours of the hot corrosion test at 950 ± 5 °C with: (a) measured thickness and (b) the EDS linear analysis

current (18 A) also has an uneven metal–shell interface that has an outer porous curved shell consisting of Fe_3O_4 and NiO phases, which make the sulfur and oxygen corrosive elements penetrate into the metal (Fig. 7e).

Based on Fig. 7c–e, as Cr and Fe oxides developed, the noble Ni component could be taken out and hence was enriched at the alloy/scale interface. Next, a layer, rich in Ni but depleted in Cr, was created as the sublayer, close to the oxide layer. The creation of oxides of Cr, Fe and other minor oxidizable elements decreased the activity of oxygen, which caused an increase in sulfur activity and speeded up a decrease in sulfur from Na_2SO_4 (Ref 36) as a result. In addition, increase in thickness of oxide layers made the rate of corrosion increase for T_4 and T_5 samples (Fig. 4).

Figure 4 and 7f shows that the corrosion product of the filler metal sample is the spinel phase of NiCr_2O_4 , which has a significant effect on the hot corrosion resistance. Pettit et al. (Ref 37) reported that the spinel (NiCr_2O_4) phase is formed between Cr_2O_3 and NiO layers and can prevent oxygen penetration into the substrate, thus reducing the rate of hot corrosion (Fig. 4). Due to the presence of this protective spinel layer, the sulfur and oxygen elements could not penetrate into the grain boundaries of the filler metal sample; however, the formation of the iron and nickel sulfide layers (FeS and NiS) may be considered a substrate. Kamal et al. (Ref 38) found out that the spinel oxide NiCr_2O_4 provides corrosion resistance to the coated superalloy IN825. El-Awadi et al. (Ref 39) figured out that the formation of adherent oxides of Cr_2O_3 and NiCr_2O_4 provided some resistance to oxidation.

According to Fig. 7e and f, it should be noted that Cr element was selectively oxidized during the initial stage of oxidation due to its higher activity to create stable Cr_2O_3 compared to NiO. In comparing the corroded cross section of the BM sample (Fig. 8) with the other samples, it can be found that the corrosion rate of the BM was very high (Fig. 4) so that the final thickness of 255 μm remained from the initial thickness of 600 μm after 48 hours of hot corrosion.

The outer shell of the sample with the optimal frequency (240 Hz) is a dense NiO oxide layer, which is morphologically different from the formed thick outer shell of Fe_3O_4 in sample T_2 (120 Hz); therefore, it can prevent the diffusion of oxygen and sulfur elements into the metal better (Fig. 7b and c). In fact, dissolution of the NiO oxide shell in the molten salt causes the

salt to penetrate into the shell–metal interface and makes the shell rise and separate from the substrate. According to the colorful analysis maps of sample T_3 (Fig. 9), the accumulation of chromium and nickel elements can be observed in the inner shell and the metal–shell interface, indicating the formation of alternate resistant oxide layers, which are able to prevent the penetration of sulfur and oxygen elements into the grain boundaries of the weld metal and restrict the corrosive elements in the outer shell of corrosion products. The analysis map of the filler metal (Fig. 10) shows the accumulation of chromium and nickel elements in the shell and in the metal–shell interface; by forming alternate protective oxide layers and spinel phase between them, it could prevent the penetration of sulfur and oxygen elements and exhibit the least amount of destruction among other samples. Figure 11 shows cobalt with purple color in the metal–shell interface, which indicates the strong presence of cobalt to reduce the hot corrosion resistance of the BM sample. Moreover, lack of formation of the dense and sticky oxide layer (Cr_2O_3) made the sulfur element easily pass through it and penetrate into the grain boundaries of N155 superalloy and form sulfide compounds there.

Although the chemical composition of the weld metal and corrosive environment conditions of the specimens are identical, the differences in the morphology and chemical composition of the corrosion products of the welded specimens can be attributed to the difference in the frequency of pulse current, which causes the difference in the microstructure and distribution of the alloying elements in the weld metal.

There is a research in which thin sheets of N155 superalloy with austenitic nickel base filler metal (Inconel 718) were welded by different frequencies of the pulsed current system (Ref 26). The results of the research illustrate that the pulse current frequency could have a significant effect on the microstructure, the mechanical properties of the joint, and the distribution of alloying elements in the fusion zone (Ref 26). Based on this research, the optimum frequency (240 Hz) in sample T_3 caused fine grains, non-segregation, and uniform distribution of alloying elements in the fusion zone among other samples (Ref 26). Liu et al. (Ref 40) figured out an improvement in the corrosion resistance of $\text{Ni}_{50.5}\text{Ti}_{49.5}$ and $\text{Ni}_{45.6}\text{Ti}_{49.3}\text{Al}_{5.1}$, which are obviously both crystalline alloys due to having grains, in NaCl electrolytes because of decreasing grain size. In fact, they realized that enhancements in

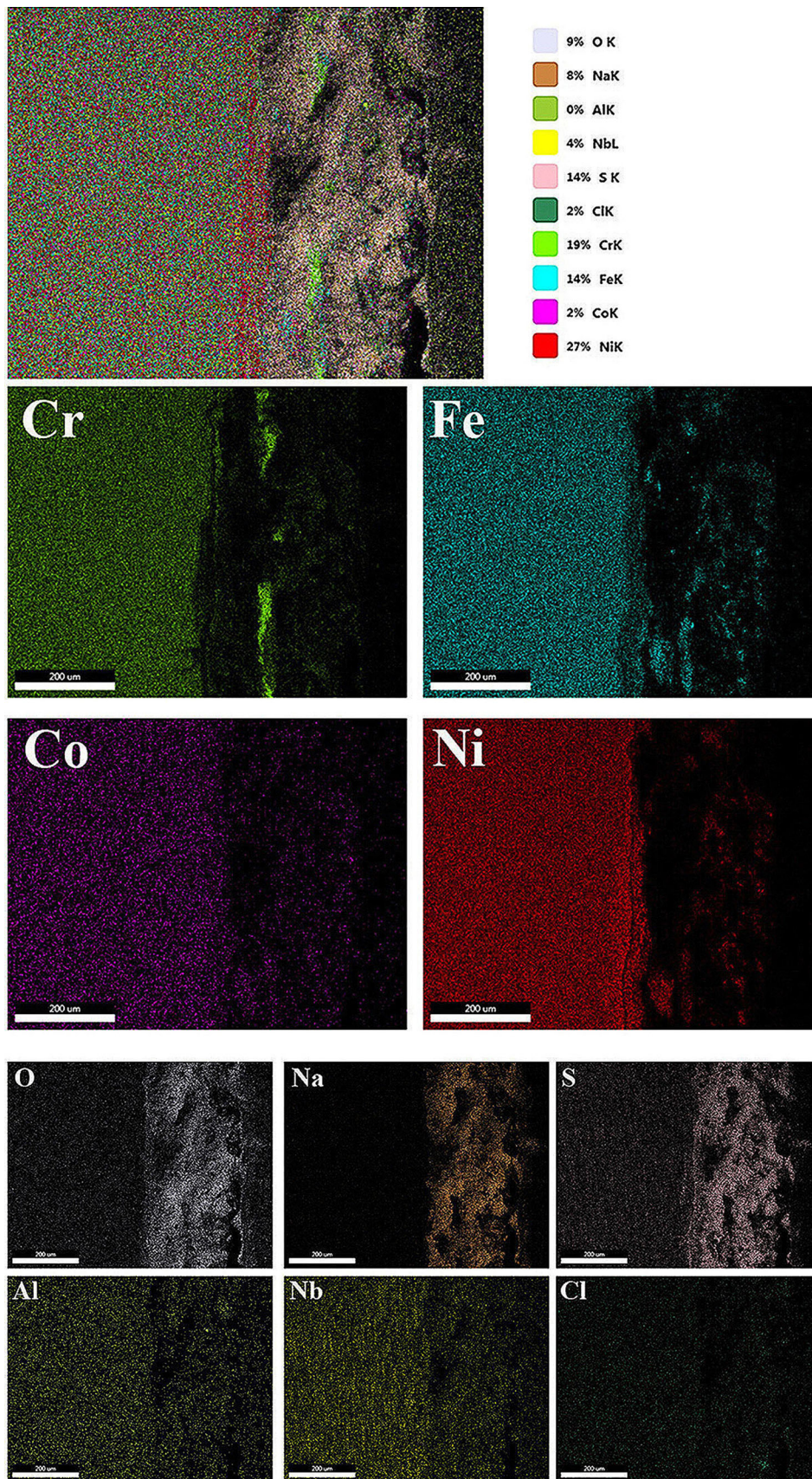


Fig. 9 Distribution of alloying elements by the EDS analysis maps of sample T_3 (240 Hz) after 48 hours at 950 ± 5 °C

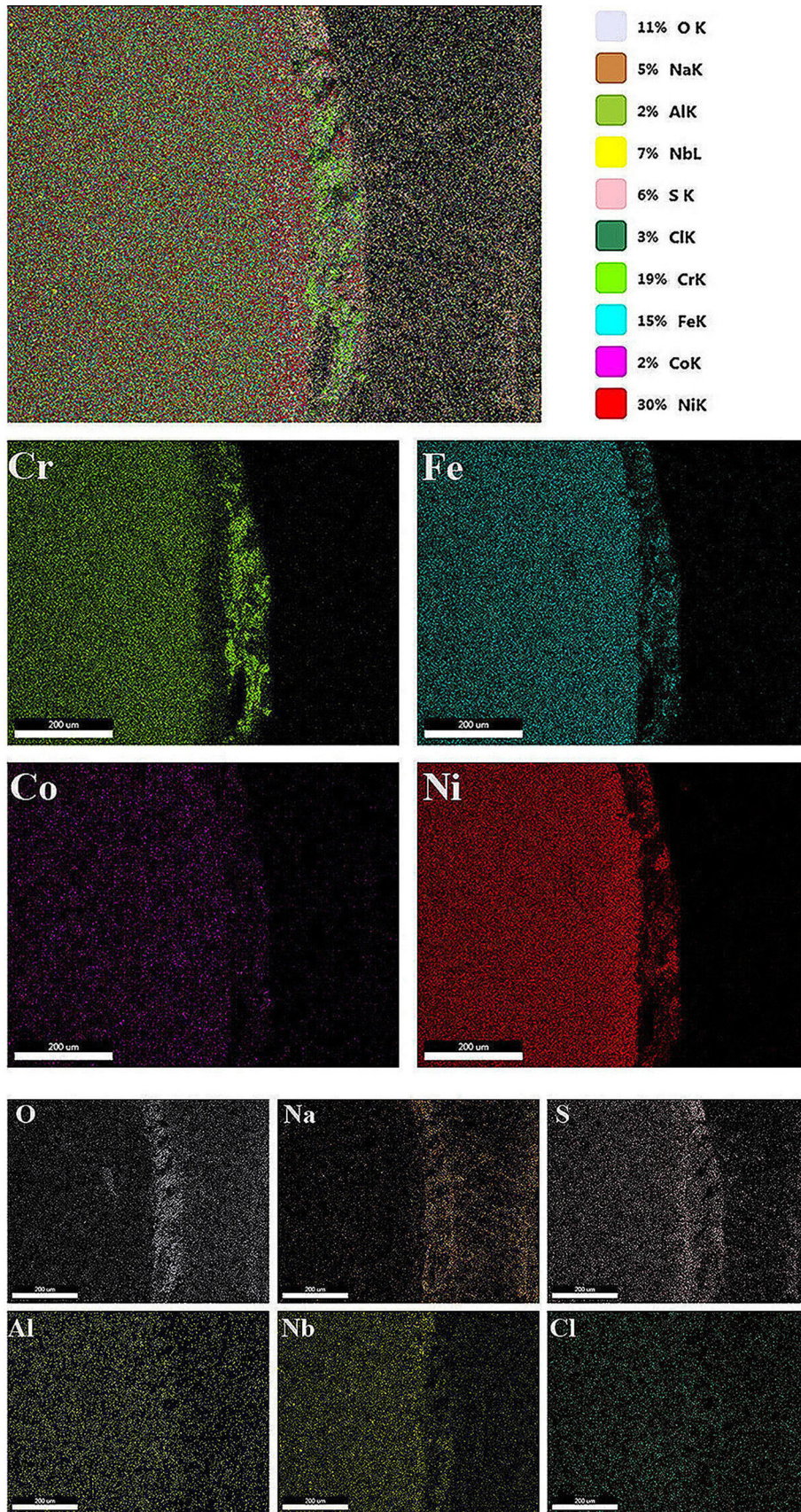


Fig. 10 Distribution of alloying elements by the EDS analysis maps of the filler metal sample after 48 hours at 950 ± 5 °C

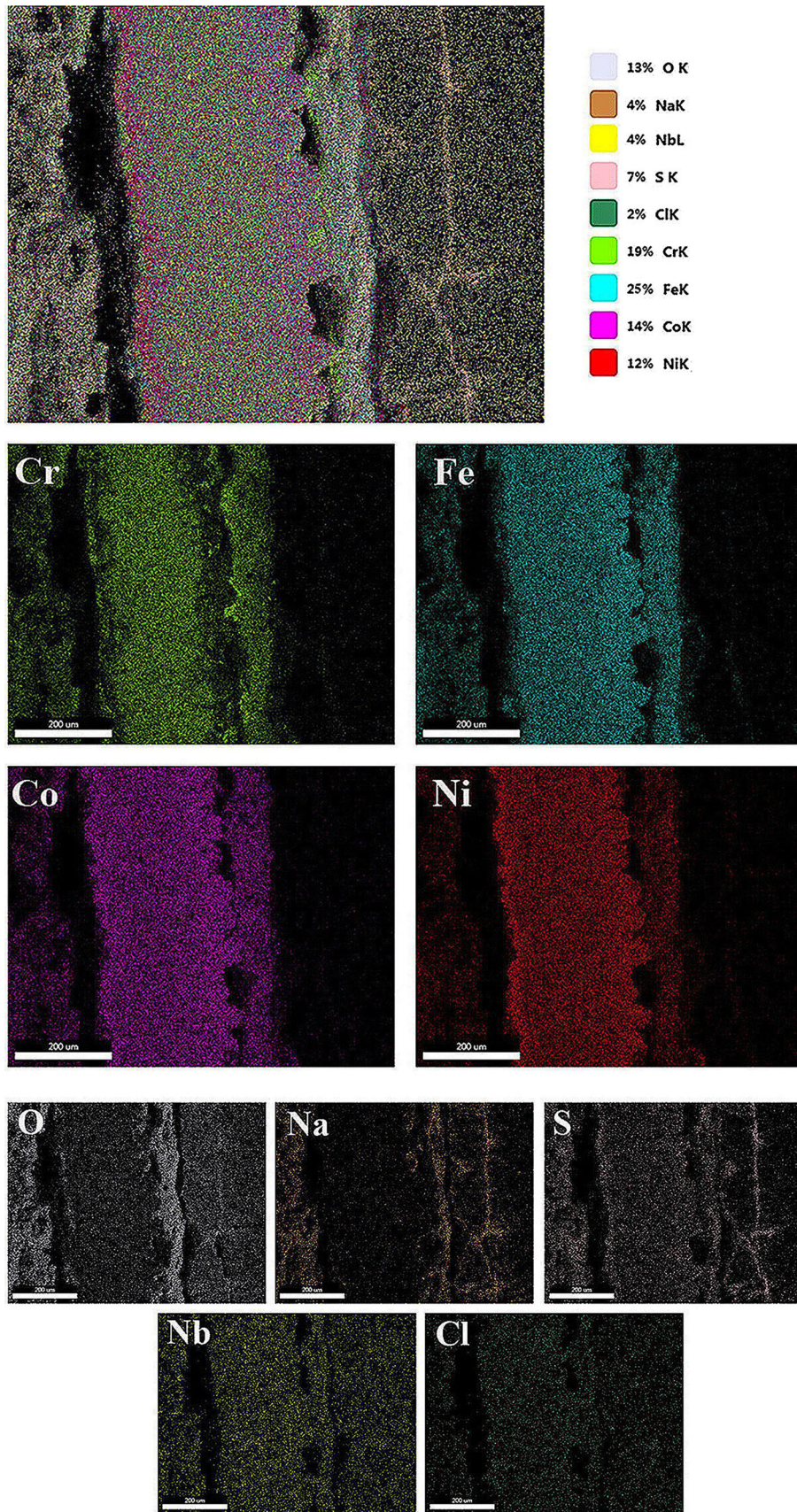


Fig. 11 Distribution of alloying elements by the EDS analysis maps of the base metal sample after 48 hours at 950 ± 5 °C

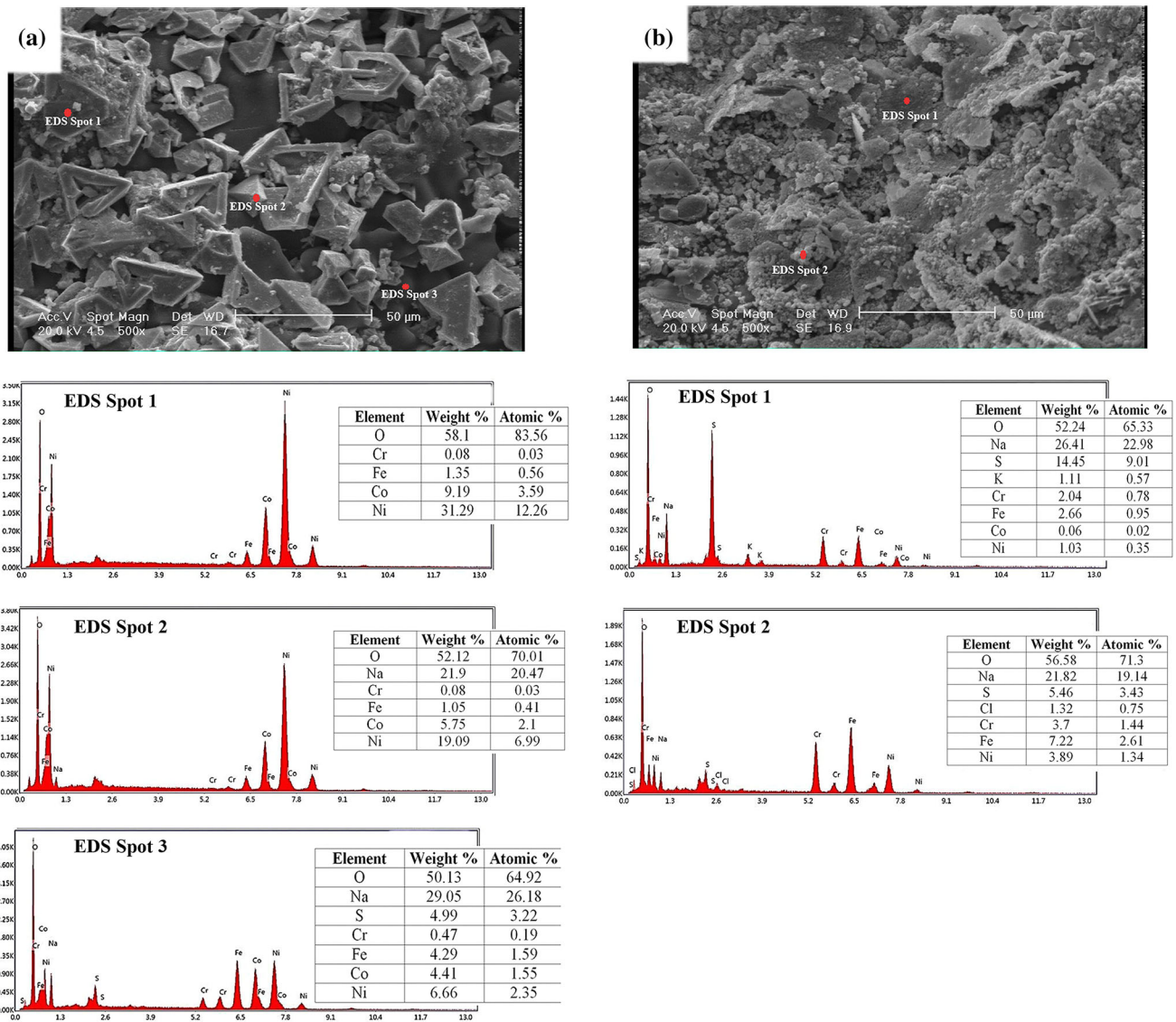


Fig.12 SEM image of the hot corrosion products after 48 hours at 950 ± 5 °C with the EDS spot analysis of; (a) T_3 (240 Hz), (b) filler metal

corrosion resistance were related to a high density of grain boundaries, which allow faster diffusion and oxide creation (Ref 40). Any modification or grain refinement that changes the reactivity of a surface will influence the corrosion performance (Ref 41). The main reason for enhancements in corrosion resistance for grain-modified materials is connected to a progress in passive film creation and adhesion because of increased grain boundary density (Ref 41). Thus, the weld metal of sample T_3 with a uniform chemical composition in the face of hot corrosion phenomenon could provide a uniform metal-shell interface, but in other welded specimens, due to the formation of poor and rich areas of chromium and nickel key elements, resulting from elements segregation of welding solidification, the weld metal surface was not uniformly corroded, which is non-smooth.

According to the EDS linear analysis of the samples, a higher percentage of nickel and chromium elements in sample T_3 was able to form the alternate protective layers (Cr_2O_3 and NiO) that prevented the interference of the iron element during the hot corrosion process; hence, the amount of damage to the substrate was reduced. Cr basically provides two purposes:

creating solid-solution strength and enhancing the corrosion and oxidation resistance. It has excellent oxidation resistance, good high temperature strength and flexibility (Ref 42).

In general, hot corrosion can be divided into two types: the first and second types depend on the environment temperature of superalloys application. In the first type of hot corrosion, the working temperature of a superalloy is about 850-950 °C, which is present in environments such as gas turbines or the oil and gas industry (Refs 10, 43). Sodium sulfate salt (Na_2SO_4) is highly corrosive and melts at about 880 °C in these environments (Refs 11, 43). Type II of hot corrosion occurs in the temperature range of 650-800 °C, which is lower than type I (Refs 44-46). Sodium sulfate salt (Na_2SO_4) is combined with other elements to form a eutectic compound that reduces the melting temperature of the salt, causing a hot corrosion attack. For example, it has been reported that cobalt is combined with Na_2SO_4 to form $CoSO_4-Na_2SO_4$, which has a melting point of about 565 °C (Refs 44-46).

According to Fig. 8a, the cracks can be detected on the surface, and some corrosion products are laminated off, which is consistent with the analysis of the kinetics of hot corrosion

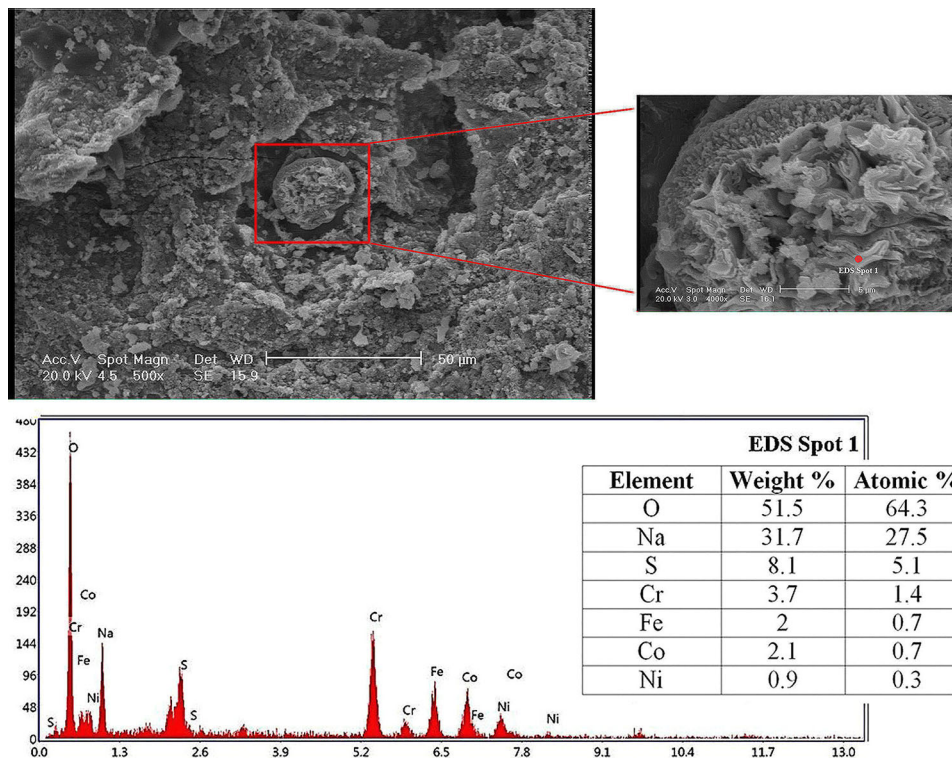


Fig.13 SEM image of the hot corrosion products of the base metal sample after 48 hours at 950 ± 5 °C with the EDS spot analysis

(Fig. 4). Based on the EDS linear analysis of corroded cross section of the base metal (Fig. 8b), type II of hot corrosion can be considered because of the high percentage of cobalt element that has an important effect on the hot corrosion mechanism. It should be noted that type II of hot corrosion occurs in the temperature range of 650 to 750 °C, but the smeared samples by the salt spent the necessary time to achieve the temperature of 950 ± 5 °C in the furnace; therefore, some effects of cobalt can be explained by the introduced Luthra mechanism (Ref 47) in which cobalt first reacts with sodium sulfate Na_2SO_4 to create the eutectic compound of $\text{Na}_2\text{SO}_4\text{-CoSO}_4$ with a melting point of about 565 °C. Then, it is melted in the furnace temperature; after decomposition of CoSO_4 , Co^{2+} ions are released and penetrate toward the metal-shell interface, and it prevents the formation of the protective layer of Cr_2O_3 (Ref 47). Zhao et al (Ref 48) found out that the elements of Co and Cr enhanced the corrosion resistance of Inconel alloy 740, and the rapid depreciation of corrosion resistance of the superalloy could be attributed to the dissolution of the protective oxide. Cobalt base alloys require at least 25% of chromium element to resist hot corrosion (Ref 3).

According to the images of the corroded cross sections at 48 hours (Fig. 7a-f and 8), it can be seen that the corrosion products consist of two layers: the thick outer porous layer and the inner thin dense layer that cover the surfaces. The typical microstructure for high-temperature hot corrosion indicates the formation of sulfides and a corresponding depletion of the reactive component in the alloy substrate. The external corrosion products often include oxide precipitates dispersed in the salt film [32, 49].

There is a general agreement that condensed alkali metal salts including (especially) Na_2SO_4 , which is a prerequisite to hot corrosion (Ref 50). The salt used in this study consisted of 90% Na_2SO_4 and 10% NaCl. The purpose of using NaCl salt

was to increase the hot corrosion rate due to the relative resistance of the filler metal and to reduce the melting point of the salt solution. However, due to the low resistance of the BM to hot corrosion in the sulfide environment, low NaCl content was used. One of the most important effects of this salt on the alloy is to increase the tendency of the oxide shells to flake and crack, which results in the rapid pick-up of chromium greatly accelerating the propagation stage. Other features include the formation of large cavities on the alloy surface; however, according to the EDS linear analysis of all the samples, due to the very low percentage of NaCl salt, its effect is not clearly observed.

The corrosion products of sample T_3 can be seen as geometrical morphologies of the prism and pyramid (Fig. 12a). Based on the atomic percentages of EDS point analysis at various points (Fig. 12a), at point 1, it shows a high percentage of NiO and a little CoO and other elements like chromium and iron also have small percentages. At point 2, the high percentage of sodium element can indicate the sodium oxide phase of Na_2O and a small percentage of the nickel and cobalt oxide phases that are present in this compound as well. At point 3, similar to point 2, a high percentage of Na_2O is present with a small percentage of sulfur oxide. Overall, it can be concluded that, as mentioned above, NiO is found as the dominant product with geometrical morphologies of the prism and pyramid, and the percentage of iron in the product is minor.

The SEM image of the corrosion products of the filler metal sample (Fig. 12b) indicates that the morphology of the phases is quite different from that of sample T_3 , and the corrosion product is seen as layered. According to the atomic percentage of EDS point analysis (Fig. 12b), point 1 shows a high percentage of Na_2O with sulfur oxide. Point 2, similar to point 1, indicates very small amounts of iron, chromium and nickel oxides, which determine the high resistance of the oxide layers

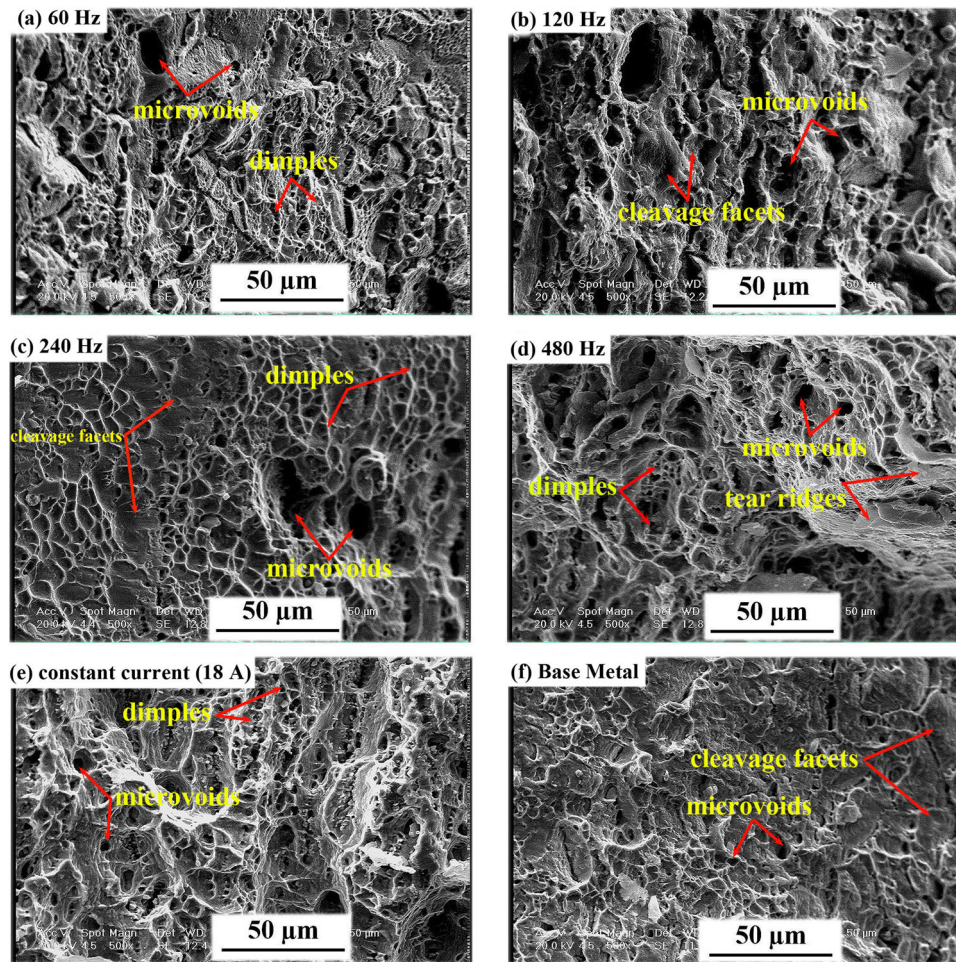


Fig.14 SEM images of the fracture surface of (a) T_1 (60 Hz), (b) T_2 (120 Hz), (c) T_3 (240 Hz), (d) T_4 (480 Hz), (e) T_5 (constant current (18 A)), (f) base metal

Table 5. Measurements related to the average size of dimples by Image-J software (Ref 26)

Sample	The average size of dimples, (μm)
T_1	15 ± 0.6
T_2	16 ± 0.7
T_3	10 ± 0.4
T_4	15 ± 0.7
T_5	15 ± 0.8
BM	8 ± 0.3

(Cr_2O_3 and NiO). The corrosion products of the base metal sample (Fig. 13) have unique morphologies; for example, the particular component was indicated at 4000 times magnification, resembling a cauliflower.

5. 5 Fractography analysis

According to Fig. 14a-e, the fracture surfaces of all specimens are soft fracture, and different dimples in size and depth can be seen (Table 5) (Ref 26). According to Fig. 14 (a,b,d,e), the fracture zones of samples T_1 (60 Hz), T_2 (120 Hz),

T_4 (480 Hz) and T_5 (constant current (18 A)) show ductile dimple tearing and trans-granular cleavage facets with tear ridges. In samples T_3 (240 Hz) and base metal, small size dimples (10 ± 0.4 and 8 ± 0.3 μm , respectively) were noticed compared to the other samples (Table 5). Moreover, the large area of ductile dimples with the almost negligible amount of cleavage facets could be seen in the fracture zone of samples T_3 (240 Hz) and base metal. Pandey et al. (Ref 51) found that connection of micro-voids leads to equiaxed dimples on tensile fracture surface normal to the loading axis, indicating the spherical and equiaxed dimples on a flat crater bottom loaded in tension test and elongated ellipsoidal dimples on the shear lips directed to 45° .

6. Conclusion

The hot corrosion examinations in the molten sodium sulfate salt at 950 ± 5 $^\circ\text{C}$ revealed that

- The weld fabricated in the optimum frequency (240 Hz) exhibited alternate resistant oxide layers (NiO and Cr_2O_3), which are able to prevent the penetration of sulfur and oxygen elements into the grain boundaries of the weld metal and restrict the corrosive elements in the outer shell

of corrosion products.

- In other welded specimens, due to the formation of poor and rich areas of chromium and nickel key elements, resulting from elements segregation of welding solidification, the weld metal surface was not uniformly corroded, which is non-smooth.
- The strong presence of cobalt element in the base metal specimen caused lack of formation of the dense and sticky oxide layers (NiO and Cr₂O₃), which made the sulfur element easily pass through it and penetrate into the grain boundaries of N155 superalloy and form sulfide compounds there.
- In the filler metal sample, due to the presence of the spinel (NiCr₂O₄) phase formed between Cr₂O₃ and NiO layers, the sulfur and oxygen elements could not penetrate into the grain boundaries.

References

1. M.J. Donachie, Relationship of Properties to Microstructure in Superalloys. American Society for Metals, Superalloys Source Book 1984, 102-111
2. T.M. Pollock and S. Tin, Nickel-Based Superalloys for Advanced Turbine Engines: Chemistry, Microstructure and Properties. *J. Propuls. Power*, 2006, 22(2), p 361-374
3. N. Eliaz, G. Shemesh and R. Latanision, Hot Corrosion in Gas Turbine Components, *Eng. Fail. Anal.*, 2002, 9, p 31-43
4. S. Kamal, R. Jayaganthan and S. Prakash, High Temperature Cyclic Oxidation and Hot Corrosion Behaviours of Superalloys at 900 C, *Bull. Mater. Sci.*, 2010, 33(3), 299-306
5. T. Hejwowski, Investigations of Corrosion Resistance of Fe- Ni-and Co-based hardfacings, *Vac.*, 2006, 80(11-12), 1386-1390
6. T.S. Sidhu, S. Prakash and R.D. Agrawal, Hot Corrosion Behaviour of HVOF-Sprayed NiCrBSi Coatings on Ni-and Fe-Based Superalloys in Na₂SO₄-60% V₂O₅ Environment at 900° C, *Acta Mater.*, 2006, 54(3), 773-784
7. H. Ahluwalia, ASM Specialty Handbook: Nickel, Cobalt, and Their Alloys. *Corrosion*, 2002, 58(4), 381
8. G. Coates, (2002) Casti handbook of stainless steels and nickel alloys, CAST1 Publishing INC: Alberta
9. A. Galerie, *High Temperature Corrosion of Chromia-Forming Iron, Nickel and Cobalt-Base Alloys*, Elsevier, NewYork, 2010
10. G.Y. Lai, High Temperature Corrosion of Engineering Alloys, 1990
11. T.S. Sidhu, Cyclic Oxidation Behavior of Ni-and Fe-Based Superalloys in Air and Na₂SO₄-25% NaCl Molten Salt Environment at 800 C, *Int. J. Phys. Sci.*, 2006, 1(1), 27-33
12. C.A.C. Sequeira and M.G. Hocking, Hot Corrosion of Nimonic 105 in Sodium Sulfate-Sodium Chloride Melts, *Corrosion*, 1981, 37, 392-407
13. I. Gurrappa, Influence of Alloying Elements on Hot Corrosion of Superalloys and Coatings: Necessity of Smart Coatings for Gas Turbine Engines, *Mater. Sci. Technol.*, 2003, 19, 178-183
14. G.S. Mahobia, Neeta Paulose and Vakil Singh, Hot Corrosion Behavior of Superalloy IN718 at 550 and 650° C, *J. Mater. Eng. Perform.*, 2013, 22, 2418-2435
15. V. Mannava, A.S. Rao, N. Paulose, M. Kamaraj and R.S. Kottada, Hot Corrosion Studies on Ni-Base Superalloy at 650_C Under Marine-like Environment Conditions Using Three Salt Mixture (Na₂SO₄+NaCl+NaVO₃), *Corros. Sci.*, 2016, 105, 109-119
16. M.S. Doolabi, B. Ghasemi, S.K. Sadmezhaad, A. Habibollahzadeh and K. Jafarzadeh, Hot Corrosion Behavior and Near-Surface Microstructure of a Low-Temperature High-Activity Cr-Aluminide Coating on Inconel 738LC Exposed to Na₂SO₄, Na₂SO₄ + V₂O₅, and Na₂SO₄ + V₂O₅ + NaCl at 900°C, *Corros. Sci.*, 2017, 128, 42-53
17. Dhananjay Pradhan, G.S. Mahobia, K. Chattopadhyay and V. Singh, Effect of Surface Roughness on Corrosion Behavior of the Superalloy IN718 in the Simulated Marine Environment, *J. Alloys Compd.*, 2018, 740, 250-263
18. D. Pradhan, G.S. Mahobia, K. Chattopadhyay and V. Singh, Severe Hot Corrosion of the Superalloy IN718 in Mixed Salts of Na₂SO₄ and V₂O₅ at 750° C, *J. Mater. Eng. Perform.*, 2018, 27, 4235-4243
19. A. Srikanth and M. Manikandan, Development of Welding Technique to Avoid the Sensitization in the Alloy 600 by Conventional Gas Tungsten Arc Welding Method, *J. Manuf. Process.*, 2017, 30, 452-466
20. K. Devendranath Ramkumar, A. Chandrasekhar, A.K. Singh, S. Ahuja and N. Arivazhagan, Effect of Filler Metals on the Structure-Property Relationships of Continuous and Pulsed Current GTA Welds of AISI 430 and AISI 904L, *Metallogr. Microstruct. Anal.*, 2015, 4, 525-541
21. M. Manikandan, N. Arivazhagan, M.N. Rao and G.M. Reddy, Microstructure and Mechanical Properties of Alloy C-276 Weldments Fabricated by Continuous and Pulsed Current Gas Tungsten Arc Welding Techniques, *J. Manuf. Process*, 2014, 16, 563-572
22. A. Rahimi and M. Shamanian, A Comparative Study on Direct and Pulsed Current Micro-Plasma Arc Welding of Alloy Ti-6Al-4V, *Trans. Indian Inst. Met.*, 2018, 71(12), 3103-3110
23. A. Rahimi and M. Shamanian, The PC-GTAW of Ti-6Al-4V Thin Sheets and Its Effects on Mechanical and Microstructural Properties, *Metallogr. Microstruct. Anal.*, 2019, 8(6), 871-879
24. S. Kumar, C. Pandey and A. Goyal, A Microstructural and Mechanical Behavior Study of Heterogeneous P91 Welded Joint, *Int. J. Press. Vessel Pip.*, 2020, 185, 104128
25. M. Jula, R. Dehmlaei and S.R.A. Zaree, The Comparative Evaluation of AISI 316/A387-Gr. 91 Steels Dissimilar Weld Metal Produced by CC-GTAW and PC-GTAW Processes, *J. Manuf. Process.*, 2018, 36, 272-280
26. A. Rahimi, M. Shamanian and J.A. Szpunar, Effect of Pulsed Current Frequency on Microstructure and Mechanical Properties of Gas-Tungsten-Arc-Welded Joints of UNS R30155, *J. Mater. Eng. Perform.*, 2020, 29(4), 2635-2647
27. M. Shamanian, A. Rahimi and J.A. Szpunar, Characterization of Microstructure and Texture across N155 Superalloy Weldment Joint with Austenitic Filler Metal, *J. Mater. Eng. Perform.*, 2020, 29, 1964-1973
28. N.B. Pilling, The Oxidation of Metals at High Temperature, *J. Inst. Met.*, 1923, 29, 529-582
29. G.Y. Lai, High Temperature Corrosion and Materials Applications, ASM International: Geauga, 2007
30. C. Greskovich, Kinetics of NiCr₂O₄ Formation and Diffusion of Cr³⁺ Ions in NiO, *J. Am. Ceram. Soc.*, 1970, 53, 498-502
31. J.A. Goebel and F.S. Pettit, Na₂SO₄-Induced Accelerated Oxidation (Hot Corrosion) of Nickel, *Metall. Trans.*, 1970, 1(7), 1943-1954
32. R.A. Rapp and Y.S. Zhang, Hot Corrosion of Materials: Fundamental Studies, *Jom*, 1994, 46(12), 47-55
33. G.S. Mahobia, N. Paulose and V. Singh, Hot Corrosion Behavior of Superalloy IN718 at 550 and 650° C, *J. Mater. Eng. Perform.*, 2013, 22(8), 2418-2435
34. R.A. Rapp, Hot Corrosion of Materials: A Fluxing Mechanism, *Corros. Sci.*, 2002, 44, p 209-221
35. T.B. Zhang, R.F. Dong, H.U. Rui, H.C. Kou and J.S. Li, Hot Corrosion Characteristics of Ni-20Cr-18W Superalloy in Molten Salt, *Trans. Nonferr. Metals Soc. China*, 2015, 25(11), 3840-3846
36. Z.Q. Hu, X.M. Lou, W.R. Sun, L.X. Yu, S.L. Yang, and W.H. Zhang, Effect of phosphorous on microstructure and mechanical properties of IN718 alloy after hot corrosion and oxidation, 7th International Symposium on Superalloy 718 and Derivatives, 2010, 961-976
37. F. Pettit, Hot Corrosion of Metals and Alloys, *Oxid. Met.*, 2011, 76, 1-21
38. S. Kamal, R. Jayaganthan and S. Prakash, High Temperature Cyclic Oxidation and Hot Corrosion Behaviours of Superalloys at 900° C, *Bull. Mater. Sci.*, 2010, 33(3), 299-306
39. G.A. El-Awadi, S. Abdel-Samad and E.S. Elshazly, Hot Corrosion Behavior of Ni Based Inconel 617 and Inconel 738 Superalloys, *Appl. Surf. Sci.*, 2016, 378, 224-230
40. K.T. Liu and J.G. Duh, Grain Size Effects on the Corrosion Behavior of Ni50. 5Ti49. 5 and Ni45. 6Ti49. 3Al5. 1 Films, *J. Electroanal. Chem.*, 2008, 618(1-2), 45-52
41. K.D. Ralston and N. Birbilis, Effect of Grain Size on Corrosion: A Review, *Corros.*, 2010, 66(7), 075005-075005
42. R. Hu, G.H. Bal, J.S. Li and J.Q. Zhang, Precipitation Behavior of Grain Boundary M23C6 and its Effect on Tensile Properties of Ni-Cr-W Based Superalloy, *Mater. Sci. Eng., A*, 2012, 548, 83-88

43. N. Birks, G.H. Meier and F.S. Pettit, *Introduction to the High Temperature Oxidation of Metals*, Cambridge University Press, Cambridge, 2006
44. J.R. Nicholls, Designing Oxidation-Resistant Coatings, *JoM*, 2000, **52**(1), 28–35
45. G.S. Mahobia, N. Paulose, S.L. Mannan, R.G. Sudhakar, K. Chattopadhyay, N.C.S. Srinivas and V. Singh, Effect of Hot Corrosion on Low Cycle Fatigue Behavior of Superalloy IN718, *Int. J. Fatigue*, 2014, **59**, 272–281
46. V. Mannava, A.S. Rao, N. Paulose, M. Kamaraj and R.S. Kottada, Hot Corrosion Studies on Ni-Base Superalloy at 650⁰C Under Marine-Like Environment Conditions Using Three Salt Mixture (Na₂SO₄ + NaCl + NaVO₃), *Corr. Sci.*, 2016, **105**, 109–119
47. K. Luthra, Low Temperature Hot Corrosion of Cobalt-Base Alloys: Part II, *React. Mech. Metall. Trans.*, 1982, **13**, p 1853–1864
48. S.Q. Zhao, X.S. Xie, G.D. Smith and S.J. Patel, The Corrosion of INCONEL Alloy 740 in Simulated Environments for Pulverized Coal-Fired Boiler, *Mater. Chem. Phys.*, 2005, **90**, 275–281
49. H. Singh, D. Puri and S. Prakash, An Overview of Na₂SO₄ and/or V₂O₅ Induced Hot Corrosion of Fe-and Ni-Based Superalloys, *Rev. Adv. Mater. Sci.*, 2007, **16**(1), 27–50
50. C. T. Sims, W. C. Hagel, The superall 17. Ch. 11: Hot Corrosion, 1972
51. C. Pandey, A. Giri and M.M. Mahapatra, Evolution of Phases in P91 Steel in Various Heat Treatment Conditions and Their Effect Onmicrostructure Stability and Mechanical Properties, *Mater. Sci. Eng. A*, 2016, **664**, 58–74

Publisher's Note Springer Nature remains neutral with regard to jurisdictional claims in published maps and institutional affiliations.